PHILOSOPHICAL TRANSACTIONS OF THE ROYAL SOCIETY B

Phil. Trans. R. Soc. B (2005) **360**, 881–891
doi:10.1098/rstb.2005.1650
Published online 29 May 2005

Validation of *q*-ball imaging with a diffusion fibre-crossing phantom on a clinical scanner

Muriel Perrin[1], Cyril Poupon[1,*], Bernard Rieul[2], Patrick Leroux[3], André Constantinesco[4], Jean-François Mangin[1] and Denis LeBihan[1,2]

[1]*Unité de Neuroradiologie Anatomique et Fonctionnelle, Service Hospitalier Frédéric Joliot, CEA SHFJ UNAF,* [2]*Institut Fédératif de Recherche 49, 4 Place du Général Leclerc, 91400 Orsay, France*
[3]*General Electric Healthcare, 283 rue de la Minière, 78533 Buc, France*
[4]*CHU Hautepierre, 1 avenue Molière, 67098 Strasbourg, France*

Magnetic resonance (MR) diffusion imaging provides a valuable tool used for inferring structural anisotropy of brain white matter connectivity from diffusion tensor imaging. Recently, several high angular resolution diffusion models were introduced in order to overcome the inadequacy of the tensor model for describing fibre crossing within a single voxel. Among them, *q*-ball imaging (QBI), inherited from the *q*-space method, relies on a spherical Radon transform providing a direct relationship between the diffusion-weighted MR signal and the orientation distribution function (ODF). Experimental validation of these methods in a model system is necessary to determine the accuracy of the methods and to optimize them. A diffusion phantom made up of two textile rayon fibre (comparable in diameter to axons) bundles, crossing at 90°, was designed and dedicated to *ex vivo* *q*-ball validation on a clinical scanner. Normalized ODFs were calculated inside regions of interest corresponding to monomodal and bimodal configurations of underlying structures. Three-dimensional renderings of ODFs revealed monomodal shapes for voxels containing single-fibre population and bimodal patterns for voxels located within the crossing area. Principal orientations were estimated from ODFs and were compared with *a priori* structural fibre directions, validating efficiency of QBI for depicting fibre crossing. In the homogeneous regions, QBI detected the fibre angle with an accuracy of 19° and in the fibre-crossing region with an accuracy of 30°.

Keywords: *q*-ball imaging; fibre-crossing phantom; magnetic resonance imaging; structural brain connectivity; orientation distribution function; *ex vivo* validation

1. INTRODUCTION

Water molecule displacement imaging, based on diffusion nuclear magnetic resonance (NMR), dates back to the 1970s (Mansfield & Grannel 1973; Grannel & Mansfield 1975), providing a new technique for tissue microstructure investigation. It relies on the acquisition of several diffusion-weighted images resulting from the application of diffusion-sensitive gradients (Stejskal 1965). Potential clinical applications of water diffusion magnetic resonance imaging (MRI) were first suggested by LeBihan *et al.* (1986), but hardware limitations in NMR systems did not allow its clinical use until the last decade (LeBihan 1991; LeBihan & Basser 1995).

In the early 1990s, the development of new clinical systems provided with powerful gradient coils (20–40 $mT\,m^{-1}$), as well as rapid digital receiver systems (high bandwidth), combined with fast acquisition schemes, such as the echoplanar technique, enabled acceptable image resolution from 2 to 3 mm. The most successful clinical application of diffusion MRI has been brain ischemia where diffusion imaging reveals lesions much sooner than conventional T2 imaging (Moseley *et al.* 1990).

Technically, diffusion imaging requires the acquisition of a set of water diffusion sensitized images from which molecule displacement probability function is inferred. Several models of water molecule displacement have been designed during the last decade, providing significant information about the order of displacement mobility and directionality of the tissue macrostructure. A first model was introduced by Basser *et al.* (1994, 1995), relying on strong assumptions (unrestricted environment, structural homogeneity within voxels) leading to a Gaussian displacement probability function, characterized by a second-order positive symmetrical tensor, in which eigenvectors represent the three major orientations of diffusion of water molecule, and eigenvalues quantify the mobility along these axes. This model represented the first attempt at a local and structural description of the matter. The tensor model is still often used because of its simplicity and its extremely fast acquisition, requiring only seven images to get a first approximation. The diffusion tensor model provides several scalar rotationally invariant parameters among which are the mean diffusivity or apparent diffusion coefficient (ADC; LeBihan & Basser 1995), and a set of index describing the anisotropy of the underlying structure

* Author for correspondence (cpoupon@shfj.cea.fr).

One contribution of 21 to a Theme Issue 'Multimodal neuroimaging of brain connectivity'.

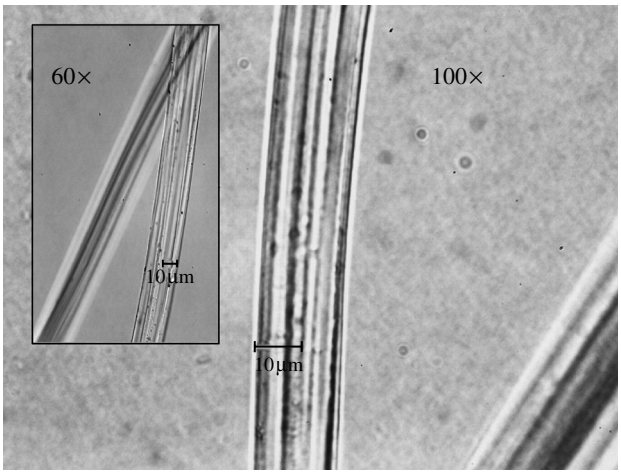

Figure 1. Microscopic view of a rayon textile filament. Rayon fibre is composed of regenerated cellulose keeping the natural permeability of cellulose and has a diameter estimated to be 17 µm, close to the myelinated axon size.

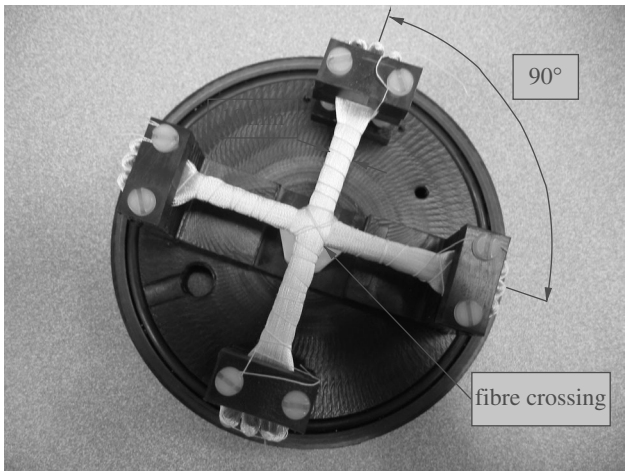

Figure 2. Top view of the phantom dedicated to diffusion high angular experiment studies. The plastic base was designed for supporting both rotating arms enabling experiments with fibre bundle crossing at different angle values. Rayon fibres organized as sheets are stacked on each other and interlaced at 90° in order to form both bundles that are tightly maintained with plastic arms, and crossing at the centre. The base and fibre bundles are placed in a glass container and filled with gas free distilled water. Each bundle has a square cross-section of 10 mm size.

(relative and fractional anisotropy; Basser & Pierpaoli 1996; lattice index and volume ratio; Pierpaoli & Basser 1996) that are quantitative and clinically relevant for brain disorder diagnostics.

A second family of parameters dedicated to tissue orientation inference was guided by a second assumption. This assumption was that anisotropy of the diffusion MR measurement, according to the diffusion sensitization, is strongly linked to the underlying structure (i.e. for brain white matter, water Brownian motion along fibres is easier than across fibres). Consequently, the orientation corresponding to the maximum diffusivity can be considered as the mean local orientation of the tissue, opening a new class of applications: inference of brain white matter connectivity or tractography (Basser 1998; Poupon *et al.* 1998, 2000; Conturo *et al.* 1999; Jones *et al.* 2000; Mori *et al.* 2000; Behrens *et al.* 2003; Tuch 2004; Parker & Alexander 2005). Connectivity knowledge is an important tool for clinicians who previously had no *in vivo* access to bundle structure offering diagnostic tools dedicated to bundle lesions, as well as for neuroscientists enabling correlation of functional and anatomical connectivity maps.

Fibre tracking helped to point out limitations of the diffusion tensor model. Despite major hardware improvements in the clinical systems, the spatial resolution of diffusion data is still several times the size of the smallest bundle size, and is a source of partial volume effects owing to multiple fibre crossing within a single voxel. Unfortunately, tensors cannot efficiently describe fibre crossing. For instance, in the case of two single bundles crossing inside a plane, an oblate tensor is obtained, where first and second eigenvectors cannot help in determining the orientations of both bundles. This situation directly affects tractography reconstructions, which usually follow the direction of the main eigenvector.

Moreover, existence of multiple compartments as well as associated restriction of diffusion cannot be ignored. Thus, both extra- and intracellular compartments characterized by their own fraction and displacement probability function must be taken into account. This observation gave rise to both classes of models dedicated either to solving fibre-crossing problems by providing a better estimation of the local displacement probability, or to the separation of intra- and extracellular diffusion components. The first idea was to consider that each bundle or compartment is characterized by its own tensor, yielding multitensorial fits (Niendorf *et al.* 1996; Pfeuffer *et al.* 1998; Tuch *et al.* 1998; Inglis *et al.* 2001; Parker & Alexander 2003; Wiegell *et al.* 2003). However, whether the non-Gaussianity is a result of intra/extracellular exchange or restriction remains unresolved. A major improvement was reached with the introduction of *q*-space imaging (QSI) making the displacement probability an inverse Fourier transform of the MR diffusion signal with respect to the displacement wave vector $\boldsymbol{q}$ (Callaghan 1988, 1991; Gory & Garroway 1990; Assaf & Cohen 1999). The lack of understanding about the diffusion process would make *q*-space the model of choice if not for two limitations. First, the Fourier relationship relies on very short duration and high amplitude diffusion gradients in order to obtain accurate Brownian displacements, which are usually not feasible on a clinical scanner. Second, *q*-space spectroscopy requires a large amount of data, considerably increasing the acquisition time, thus preventing its clinical use. However, the *q*-space formalism assisted understanding of tensor models (Basser 2002), defining more realistic models at high angular resolution. Several high angular resolution descriptions of the diffusion function have been recently developed without any *a priori* knowledge about the underlying angular structure, such as maximum entropy solutions (Alexander & Jansons 2002), or methods inherited from QSI, such as diffusion spectrum imaging (DSI), *q*-ball imaging (QBI; Tuch 2002, 2004) or spherical deconvolution (Tournier *et al.* 2004). The former models give access

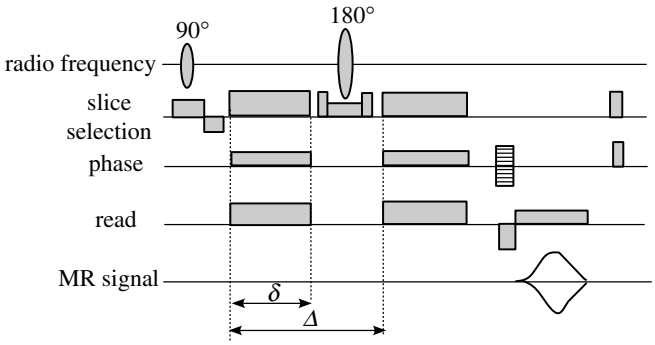

Figure 3. Diffusion pulsed-gradient spin echo sequence. Diffusion sensitization is performed with a standard Stejskal–Tanner's pair of displacement encoding gradients. Sequence parameters were as follows: field of view, FOV = 19 cm; slice thickness, TH = 3 mm; 128 × 96 matrix; echo time, TE = 52 ms; repetition time, TR = 1000 ms; diffusion sensitization, $\delta = 21.52$ ms/$\Delta = 26.06$ ms/$G = 40$ mT m^{-1}.

to the orientation distribution function (ODF). This information is less complete than the displacement probability, but it is still suitable for the inference of multiple fibre directions within a single voxel.

Most models have been validated by software simulations and their efficiency has been demonstrated *in vivo* on experiments with healthy volunteers or animals when acquisition time could not allow it.

Ex vivo validation is also a crucial step for validating models given the *a priori* knowledge of the reality. However, determining the sensitivity of the model is also important for detecting imaging artefacts and for optimizing acquisition. Astonishingly, few validations have been realized *ex vivo* with diffusion phantoms. Most validations concerned biexponential tensor models, dedicated to the separation of intra- and extracellular compartments, requiring multicompartmental phantoms (Pfeuffer *et al.* 1998; Assaf *et al.* 2004). Few experiments involving fibre-crossing phantoms have been realized for studying high angular resolution diffusion models. Lin and colleagues measured a fibre-crossing phantom made up of thin capillaries immersed in water, organized in interleaved sheets, with a given angle (Lin *et al.* 2003). The deviation angle between the primary and second orientations of the displacement probability function was calculated from a set of diffusion-weighted images, which was compared with both orientations of crossing capillaries. The experiment was conducted on an MR system with high gradient slew-rate and magnitude capabilities delivering 50 times more strength than a clinical gradient coil. However, no validation is yet available for QBI on a clinical scanner. Here, we present an *ex vivo* validation of QBI using a dedicated fibre-crossing phantom on a standard clinical MR system, demonstrating the adequacy of such a model for inferring the presence of several fibre populations characterized by different structural orientations.

A preliminary study was conducted concerning the choice of the material for fibres. Most studies of the literature use glass capillaries or haemodialyse plastic capillaries. Glass capillaries prevent any bending phantom, whereas haemodialyse capillaries have too large a

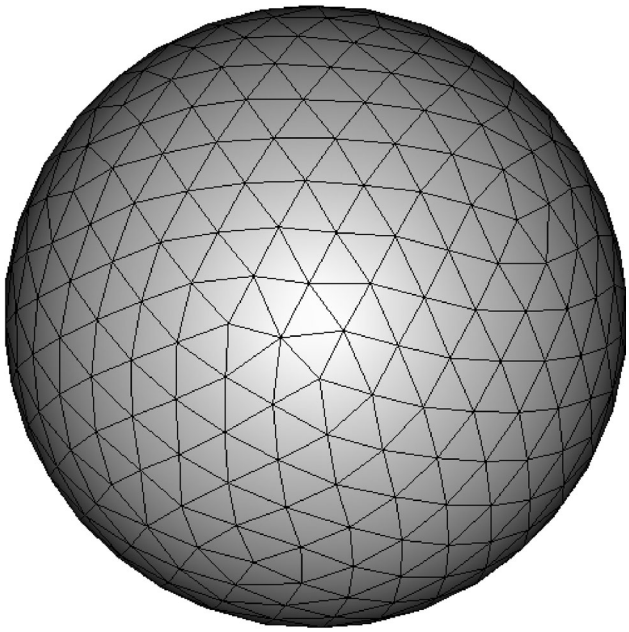

Figure 4. Diffusion orientation scheme. The three-dimensional rendering displays the 200 played orientations together with their symmetric orientations that are equivalent for the diffusion process. This quasi-uniform set was established from an electrostatic model of interactions between directions mutually repulsing.

diameter compared with the diffusion measurement scale. Consequently, plasticity, permeability and size requirements lead us to choose rayon textile filament fibre. In the production of rayon, purified cellulose extracted from trees is chemically converted to xanthate, which is dissolved in diluted caustic soda (viscose process). Cellulose is then regenerated from the solution through a spinneret (http://www.fibersource.com). Permeability is a natural property of cellulose enabling tree assimilation processes, so the first requirement is met, in spite of the fact that no quantitative value of the permeability is available from the manufacturer. For measuring the diameter of rayon filaments, a microscope was used and provided an estimated size close to 17 μm, which meets the second requirement (figure 1). Further measurements should be achieved in the future in order to characterize the variability of that diameter. Unfortunately, we did not find any tubular cellulose fibre, which would have been a perfect myelinated axon model. Nevertheless, rayon filament is a good surrogate for white matter axons because it has a comparable diameter, can be densely packed and is permeable.

2. METHODS

(a) *Phantom design*

We developed a phantom for simulating fibre crossing inside white matter. In order to be realistic, a diffusion phantom must respect several conditions that are not easily fulfilled for technical reasons. First, fibres must have a diameter close to the myelinated axon size (i.e. 10–20 μm), and must be permeable in order to allow water molecule exchange between both extra- and intracompartments. Second, the artificial fibre crossing should look like realistic anatomical situations encountered with standard diffusion-weighted imaging (i.e. with voxel resolution close to $3 \times 3 \times 3$ mm^3).

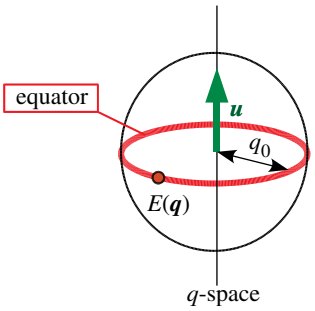

Figure 5. Funk Radon transform principle. The FRT of the MR signal $E(\boldsymbol{q})$, sampled on a sphere of radius q_0 for a given orientation $\boldsymbol{u}$ (represented in green) of the space, is equal to the integral of $E(\boldsymbol{q})$ along the equator (red ellipse) of $\boldsymbol{u}$.

As shown in figure 2, the phantom is built from several layers of parallel fibres, stacked on each other in order to form two fibre bundles of 10 mm each side. Two arms maintain the bundles, which can be rotated to set the angle to a given value starting from 30 to 90°. Each bundle is strongly tightened to provide a relatively strong local anisotropy. The whole structure is immersed in a solution of distilled water at a temperature of 20 °C. For the experiment, the angle between both bundles was set to 90°.

The quality of the water solution must also be taken into account and is strongly connected to MR signal considerations. An MR signal can be characterized by its proton density ρ, its relaxation times T1 and T2, and its apparent diffusion coefficient D (equation (2.1)). The b-value measures the diffusion sensitization

$$S = S_0(\rho)\mathrm{e}^{-\mathrm{TE/T2}}\mathrm{e}^{-bD}. \qquad (2.1)$$

In order to estimate the average value of T2 on a region of interest containing rayon fibres, spin echo acquisitions were performed with different echo times, followed by a linear fit of the T2-weighted MR signal, giving a T2 close to 90 ms. This value is not far from the white matter T2 value (80 ms), and we did not need doping water with gadolinium. It is interesting to observe that on a region of interest located in water without fibres, the T2 value is close to 1200 ms, revealing the strong effect of the underlying fibre structure on the spin-to-spin interaction. The choice of the echo time value is guided by gradient coil limitations and by diffusion sensitization settings. It was reduced to a minimum value of 52 ms (further details will be provided in §2*b*), yielding a T2 attenuation factor of 0.56.

A second set of spin echo data was acquired in order to measure the proton density decrease resulting from the use of non-tubular filaments. Measurements were taken with a short echo time (8 ms) and a long repetition time (3 s) on both regions of interest (one containing fibres, and the other containing only water), in order to evaluate the corresponding $S_0(\rho)$ values, which must be proportional to proton density. Measurements were corrected from the T2 attenuation factor. We found that the proton density inside fibres is approximately twice as low as inside pure distilled water, which is comparable to the ratio of proton density between brain grey/white matter and pure water.

As a first conclusion, the maximum MR signal magnitude (i.e. without diffusion sensitization) inside fibres can be evaluated to 25% of the MR signal measured inside pure water. This attenuation obviously reduces the signal to noise ratio (SNR), but fortunately, QBI involves many samples that help recover an adequate SNR.

The final factor that can drastically decrease the quality of MR images is the presence of air bubbles within the solution,

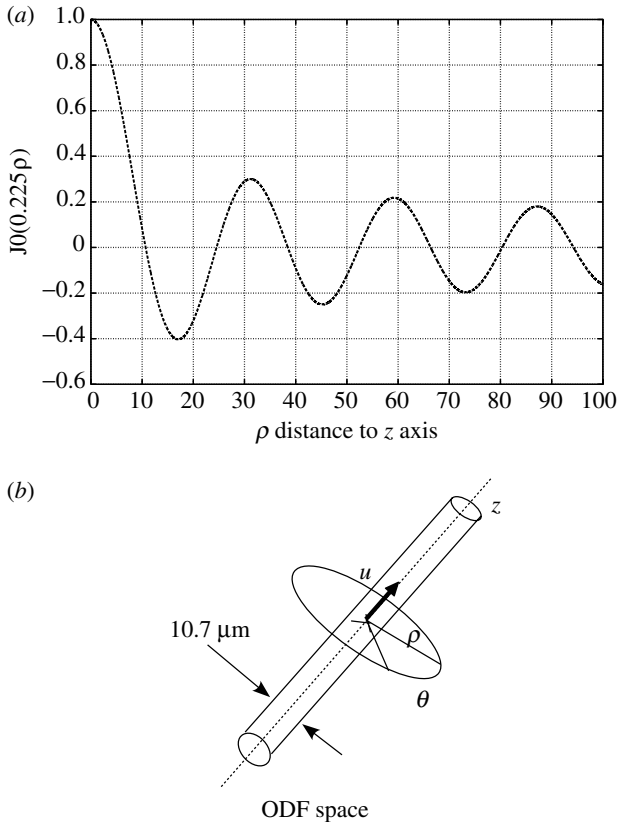

Figure 6. Impact of the regular zeroth-order Bessel function on the q-ball fundamental equation. (*a*) $\mathcal{J}_0(0.225\rho)$ Bessel function plot resulting from a diffusion sensitization of wave vector magnitude $q_0 = 3.58 \times 10^{-4}\,\mathrm{m}^{-1}$; (*b*) q-ball model approximates the spatial radial projection along $\boldsymbol{u}$-axis by the integration of the displacement probability function on a cylindrical domain with $\boldsymbol{u}$-axis and radius 10.7 µm corresponding to the width of the principal lobe of Bessel function $\mathcal{J}_0(0.225\rho)$.

which create air/water interfaces responsible for local B0 inhomogeneities that are a source of important susceptibility artefacts. Using the echoplanar acquisition technique with long echotrain, susceptibility effects result in large geometrical distortions and modifications of the signal intensity. The standard spin echo pulse sequence is less prone to susceptibility artefacts but the net dephasing of the spins may be considerably increased when too many air bubbles remain, contributing to a significant decrease of the SNR. In order to prevent such drawbacks, the solution is submitted to a specific preparation dedicated to remove putative gas bubbles that consist of a first step of degasification of distilled water under vacuum conditions, followed by a filling operation of the glass container, and, finally, with a sonication process of the solution in order to obtain an almost complete suppression of small bubbles attached to water/glass or bundle/water interfaces. The sonication process consists of plunging a beam inside water that delivers an ultrasonic wave and automatically destroys gas bubbles. This process still needs to be improved because some very small bubbles remain in the solution, such that echoplanar acquisition scheme cannot be used. Nevertheless, this limitation is not a significant issue for *ex vivo* experiments where a long acquisition time is acceptable.

(b) *Data acquisition*

We performed MRI experiments on a GE Healthcare Signa 1.5 T Excite scanner with a 40 mT m^{-1} full body gradient

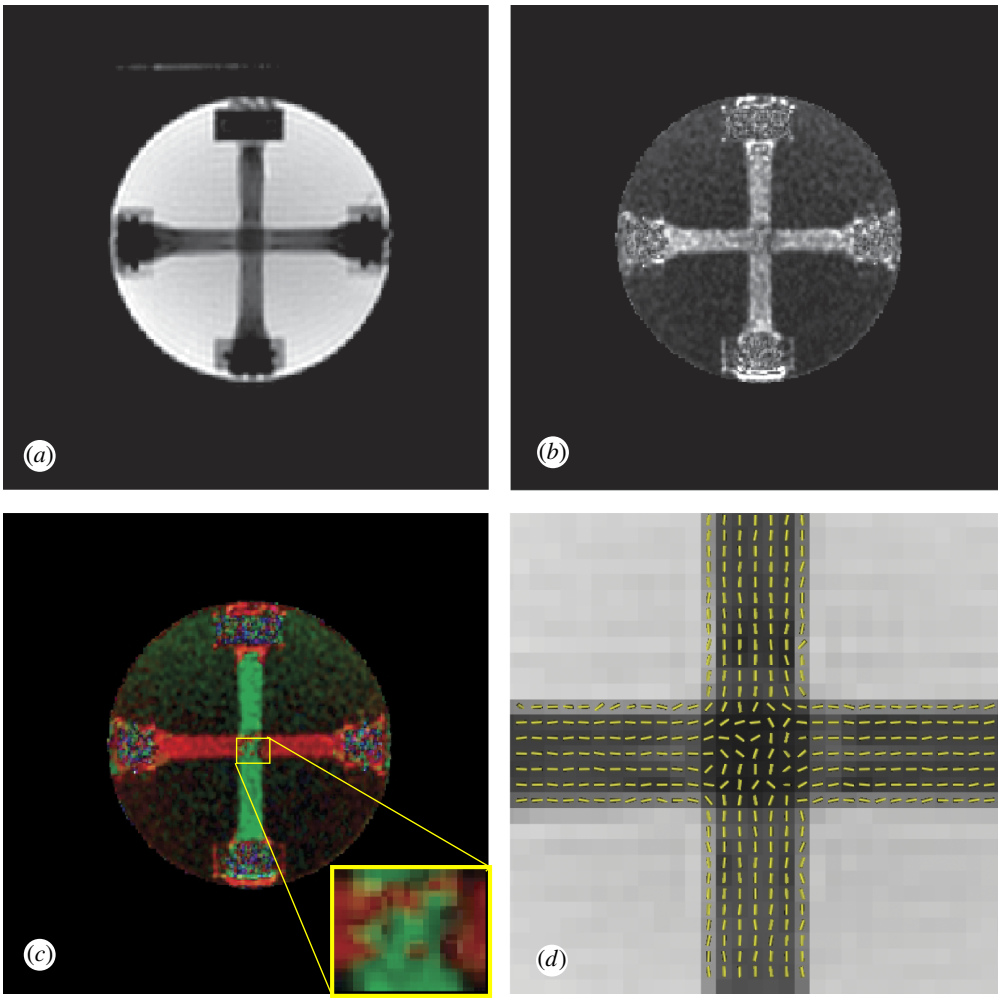

Figure 7. Axial maps of diffusion phantom corresponding to diffusion tensor model. (*a*) T2-weighted map of an axial slice located inside fibre bundles; (*b*) fractional anisotropy map revealing the anisotropy of the underlying structure; (*c*) Red–green–blue colour map asserting the presence of one fibre bundle oriented along the horizontal *x*-axis (red colour) and one fibre bundle oriented along the vertical *y*-axis (green colour); (*d*) map of the main eigenvector of diffusion tensor superimposed on the T2-weighted image. Note the mixture of red and green colour on the RGB map at the location corresponding to fibre crossing, and the wrong corresponding eigenvectors.

coil, an eight-channel acquisition system, and an eight-channel head surface coil. Data were reconstructed using a sum of squares algorithm.

We note that we used a standard scanner in order to validate QBI with a diffusion phantom under clinical imaging conditions, which is a challenging aspect of this work compared with DSI validation achieved in Lin *et al.* (2003), which was realized with a micro-gradient coil delivering up to 1000 mT m^{-1}.

As described previously, echoplanar acquisition cannot be carried out on the diffusion phantom owing to the presence of small air bubbles yielding large susceptibility artefacts. Therefore, we used a standard pulsed gradient spin echo sequence with conventional Stejskal–Tanner diffusion sensitization (Stejskal & Tanner 1965; Tanner & Stejskal 1968; figure 3).

Sequence parameters were as follows. The field of view was set to 19 cm. The slice thickness was set to 3 mm, including enough layers of rayon fibres crossing at 90°. We used a 128×96 acquisition matrix, interpolated during reconstruction to 256×256, leading to $0.74 \times 0.74 \times 3\ mm^3$ voxels, and we selected 4 interleaved axial slices parallel to the plane containing fibre bundles. Data were reinterpolated to 128×128 matrix yielding $1.5 \times 1.5 \times 3\ mm^3$ voxels.

Echo time, TE, was set to its minimum possible value 52 ms and repetition time, TR, was chosen considering T1 estimation inside fibres and set to 1000 ms. The total scan time for the dataset was exactly 5 h 36 min.

Diffusion sensitization settings were chosen within the constraints of both hardware limitations and characteristics of the anisotropic structure to be measured. Water solution is characterized by an ADC close to $2.2 \times 10^{-9}\ m^2\ s^{-1}$ at 25 °C. This value is approximately three times the value of ADC inside white matter and clinical QBI of the brain requires *b*-values greater than 3000 s mm^2 to obtain correct high angular ODF. Therefore, we decided to use a *b*-value equal to 1000 s mm^2. The gradient coil specifications of the system lead to the following Stejskal–Tanner parameters: $\delta = 21.52$ ms; $\Delta = 26.064$ ms; and $G = 40$ mT m^{-1} that correspond to the spatial modulation $|\boldsymbol{q}| = (\gamma/2\pi)\delta G = 3.58 \times 10^4\ m^{-1}$ (γ is the gyromagnetic ratio, G is the diffusion gradient magnitude corresponding to the nominal maximal gradient strength).

As the diffusion sensitization parameters are known, one can compute the free average displacement $\sigma = \sqrt{2D\tau} = 9.12\ \mu m$ with the diffusion time $\tau = \Delta - \delta/3 = 18.89$ ms. This 9.12 μm average displacement must be compared to the fibre spacing achievable with rayon fibres of 17 μm diameter and manual packing technique. A greater displacement sensitivity

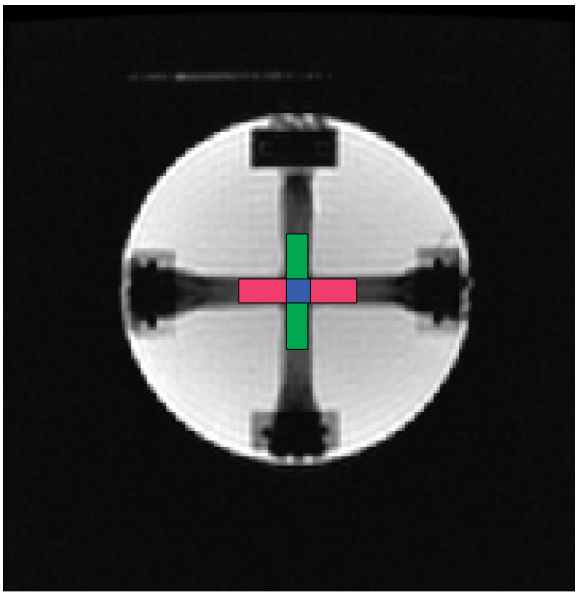

Figure 8. Definition of regions of interest from the T2-weighted image for QBI reconstruction. The red region (ROI_1) corresponds to the bundle aligned with horizontal axis. The green region (ROI_2) corresponds to the bundle aligned with vertical axis. The blue region (ROI_3) corresponds to the fibre crossing.

would have revealed more of the bundle structure anisotropy. However, it should be sufficient for estimating a correct ODF under the assumption of measurement of the diffusion centre of mass (Mitra & Halperin 1995).

QBI consists in sampling the sphere of radius $|\boldsymbol{q}|$ in the q-space. The corresponding diffusion-encoding scheme constituted 200 diffusion-encoding orientations of the $\mathcal{R}^3$ space. This quasi-uniform set of 200 orientations was built from an electrostatic model of interactions between directions, which accounts for the symmetry of diffusion process (Jones *et al.* 1999; see figure 4).

(c) *q*-Ball model

The q-ball model is inherited from q-space method, defining a Fourier relationship between the MR signal $E(\boldsymbol{q})$, acquired with a specific diffusion weighting characterized by a wave vector $\boldsymbol{q}$ (defining the spatial modulation and equal to $(\gamma/2\pi)\delta G$). The conditional displacement probability $p(\boldsymbol{r})$ for water molecules to follow a random walk of average deviation $\boldsymbol{r}$ [20][21] during a diffusion time τ (equation (2.2)) can be represented by

$$E(\boldsymbol{q}) = \int p(\boldsymbol{r},\tau)\mathrm{e}^{\mathrm{i}2\pi\boldsymbol{q}\boldsymbol{r}}\,\mathrm{d}\boldsymbol{r}. \tag{2.2}$$

To be valid, this property relies on a strong assumption, known as narrow pulse condition, imposing a Dirac shape to the diffusion gradient pulses, which is practically not feasible. However, it has been demonstrated that the use of finite gradient pulse widths leads to the true probability density function up to a scaling factor (Mitra & Halperin 1995).

The likelihood of any displacement along a specific orientation $\boldsymbol{u}$ of the space is given by the ODF (equation (2.3))

$$\mathrm{ODF}(\boldsymbol{u}) = \int_0^\infty p(r\boldsymbol{u})\mathrm{d}r. \tag{2.3}$$

The anisotropic part of the structure can be consequently defined by the min–max normalization of the ODF (equation (2.4))

$$\mathrm{ODF}_N(\boldsymbol{u}) = \frac{\mathrm{ODF}(\boldsymbol{u}) - \min_v\{\mathrm{ODF}(\boldsymbol{v})\}}{\max_v\{\mathrm{ODF}(\boldsymbol{v})\} - \min_v\{\mathrm{ODF}(\boldsymbol{v})\}}. \tag{2.4}$$

Measuring the displacement probability function with a q-space sampling requires a very long acquisition. Instead, Tuch demonstrated that another interesting relationship between diffusion MR signal and ODF can be established, providing a good ODF estimation that does not require integrating the probability density function on an unbounded domain. It is known as QBI (Tuch 2002, 2004).

The QBI reconstruction is based on the spherical or Funk Radon transform (FRT; equation (2.5)), which, for a given orientation $\boldsymbol{u}$ of the space, involves integrating the diffusion signal over the equator of $\boldsymbol{u}$ on a sphere with the radius q_0 (q_0 is the diffusion wave vector intensity; figure 5)

$$\mathrm{FRT}_{q_0}(\boldsymbol{u}) = \int E(\boldsymbol{q})\delta(\boldsymbol{q}^{\mathrm{T}}\boldsymbol{u})\delta(\|\boldsymbol{q}\| - q_0)\mathrm{d}\boldsymbol{q}. \tag{2.5}$$

Replacing $E(\boldsymbol{q})$ by the q-space equation (2.1) and using cylindrical coordinates (ρ,θ,z) instead of Cartesian coordinates in the displacement space yields the fundamental q-ball approximation of the ODF (equation (2.6)), where the z-axis corresponds to the $\boldsymbol{u}$-axis, θ is the polar angle and ρ is the distance to $\boldsymbol{u}$-axis. $\mathcal{J}_0(x)$ is the zeroth order Bessel function (figure 6)

$$\mathrm{FRT}_{q_0}(\boldsymbol{u}) = 2\pi q_0 \int p(\rho,\theta,z)\mathcal{J}_0(2\pi q_0\rho)\rho\,\mathrm{d}\rho\,\mathrm{d}\theta\,\mathrm{d}z \approx \mathrm{ODF}(\boldsymbol{u}). \tag{2.6}$$

Ideally, $\mathcal{J}_0$ should be a Dirac pulse in order to satisfy the radial projection of the ODF (equation (2.3)). If we consider the $q_0 = 3.58 \times 10^{-4}\,\mathrm{m}^{-1}$ diffusion wave vector amplitude used for the acquisition on the phantom, then the resulting Bessel function $\mathcal{J}_0(0.225\rho)$ leads to an intermediate spatial resolution $\Delta r = 2.405/(2\pi q_0) = 10.7$ μm, which seems to be a good compromise between angular resolution of the ODF and SNR. Roughly, the Bessel function can be approximated to its first lobe with a predominant action on the probability density function, ignoring the impact of secondary lobes. Thus, equation (2.6) means that the radial projection on the axis supporting $\boldsymbol{u}$ was replaced by the integration of the probability inside a cylinder of radius equal to 10.7 μm (figure 6), which can be also regarded as a partial voluming effect, resulting in a smoothing operation of the ODF surface.

The q-ball reconstruction algorithm was implemented as described in Tuch (2002), and can be downloaded with the last release of the BRAINVISA platform (Cointepas *et al.* 2003). Principle peak directions were determined with an algorithm that loops over the set of discrete orientations of the q-ball for finding the orientation corresponding to the maximum probability. Once it is detected, the set of orientations contained within a given solid angle (typically a 20–30° aperture angle) around that peak is removed from the set of available orientations to be parsed during the next iteration.

(d) *Deviation angles*

The diffusion phantom, made up of both fibre bundles crossing at 90°, was placed in the magnet in such a way that bundles are aligned with x- and y-gradient axes. Thus, the quadratic discrepancy between the primary orientation of the ODF and the x- or y-laboratory axis in regions containing one single-fibre population, or between the primary and second orientations of the ODF and both x- and y-axes in regions containing fibre crossing, can be established for benchmarking the quality of q-ball model (equation 2.7). $\boldsymbol{o}_1$ and $\boldsymbol{o}_2$ represent the primary and second orientations of the ODF. α_1, α_2 and α_3 are the quadratic angle error over domains

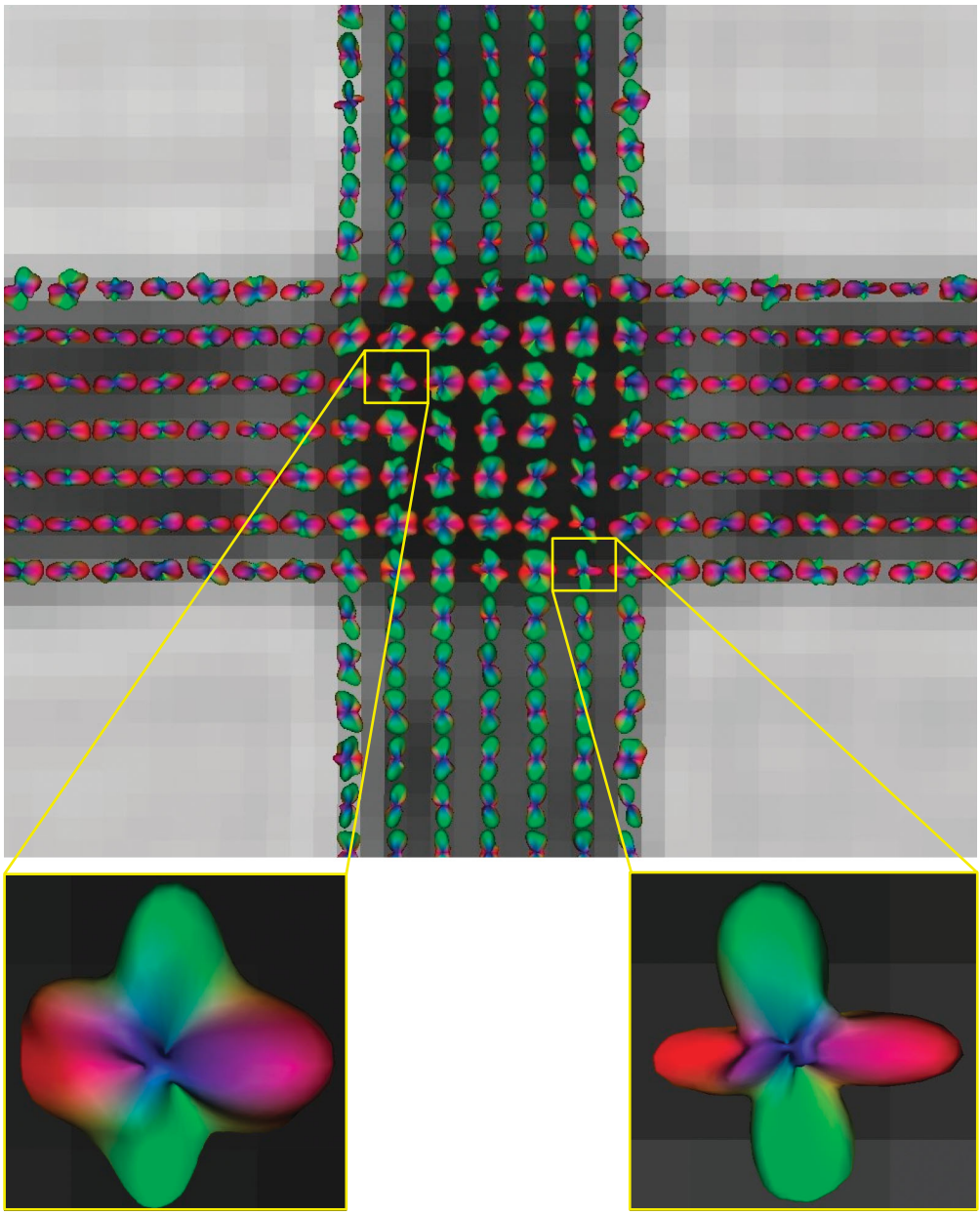

Figure 9. Three-dimensional renderings of min–max normalized ODF superimposed on T2-weighted map. ODFs were estimated from QBI method. Reconstruction parameters are described in §4. ODF patterns corresponding to ROI_1 and ROI_2 displays one lobe that is consistent with the underlying structure orientation of rayon fibres. ODF shapes inside ROI_3 clearly displays two principle orientations, as shown in zoomed renderings, aligned with horizontal and vertical axis.

ROI_1, ROI_2 and ROI_3 correspond to regions of interest containing rayon fibres aligned with the x-axis, the y-axis or both, respectively (i.e. fibre crossing; figure 8). $\boldsymbol{u}_x$ and $\boldsymbol{u}_y$ are unitary vectors aligned with the x- and y-axis

$$\left.\begin{aligned}
\alpha_1 &= \left(\frac{1}{\mathrm{card}\{\mathrm{ROI}_1\}}\sum_{\boldsymbol{p}\in\mathrm{ROI}_1}(\boldsymbol{o}_1(\hat{\mathrm{ODF}}_N(\boldsymbol{p})),\boldsymbol{u}_x)^2\right)^{1/2},\\
\alpha_2 &= \left(\frac{1}{\mathrm{card}\{\mathrm{ROI}_2\}}\sum_{\boldsymbol{p}\in\mathrm{ROI}_2}(\boldsymbol{o}_1(\hat{\mathrm{ODF}}_N(\boldsymbol{p})),\boldsymbol{u}_y)^2\right)^{1/2},\\
\alpha_3 &= \left(\frac{1}{2\mathrm{card}\{\mathrm{ROI}_3\}}\left(\sum_{i=1}^{2}\sum_{\boldsymbol{p}\in\mathrm{ROI}_3}\mathrm{argmin}_{j\in\{x,y\}}\right.\right.\\
&\qquad\left.\left.(\boldsymbol{o}_i(\hat{\mathrm{ODF}}_N(\boldsymbol{p})),\boldsymbol{u}_j)^2\right)\right)^{1/2}.
\end{aligned}\right\} \tag{2.7}$$

3. RESULTS

(a) *90° crossing phantom experiment*

The T2-weighted spin echo image shows both regions with a darker signal resulting from a lower T2 relaxation time intersecting at 90° corresponding to fibre bundles (figure 7*a*). The fractional anisotropy map is also provided in order to show the presence of anisotropy located in rayon bundles (figure 7*b*). The RGB colour map, calculated from the diffusion tensor model (Pajevic & Pierpaoli 1999), reveals the existence of three different regions: a red-coloured region corresponding to the first bundle oriented along the x-axis; a green-coloured region corresponding to the second bundle oriented along the y-axis; and a third region with alternating red/green colour corresponding to the fibre crossing, illustrating the incapacity of tensor model for describing the structure of voxels gathering more than

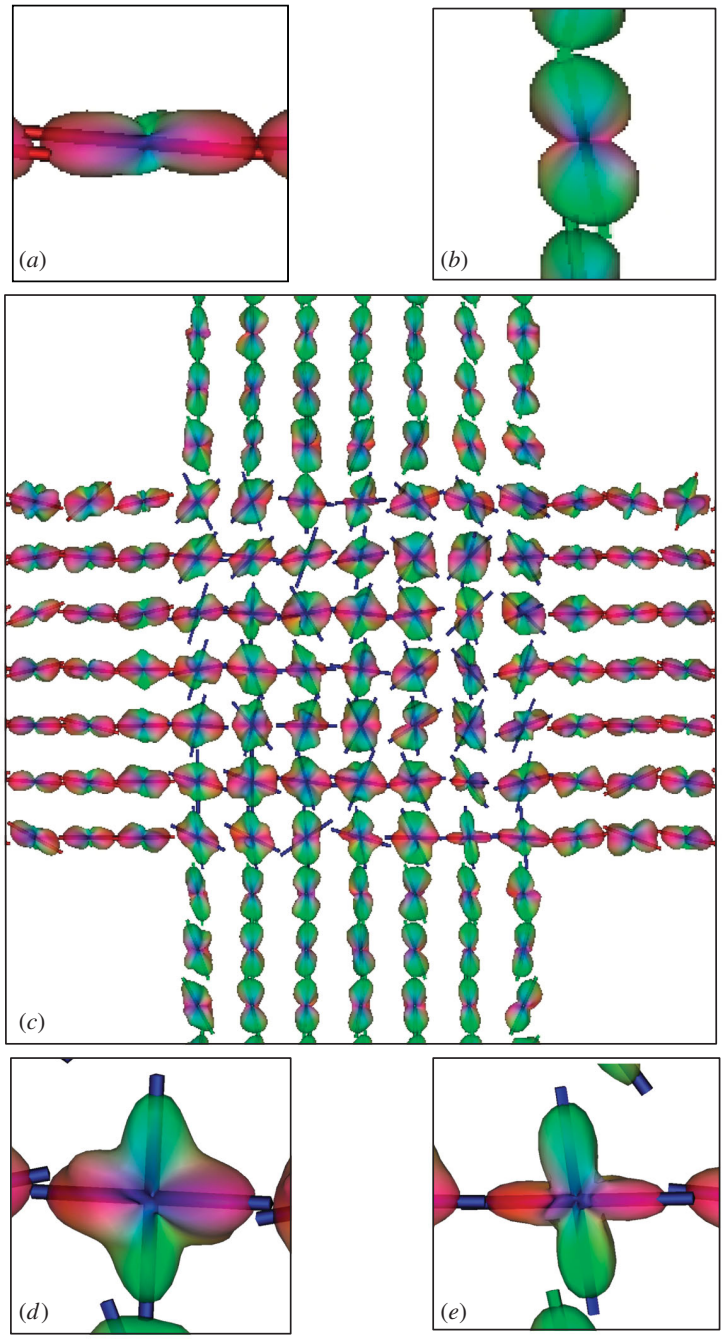

Figure 10. Fusion between transparent three-dimensional renderings of the ODF and vectors representing single or dual main orientations of the ODF (*c*) on a the whole region of interest; (*a*)–(*d*) on regions of interest ROI_1, ROI_2 and ROI_3, respectively.

one population (figure 7*c*). The map of principle eigenvectors depicts the poor estimation of the structure orientation from diffusion tensor imaging (DTI) for fibre-crossing regions, and some good results for regions containing only one population of fibres (figure 7*d*).

Three regions of interest were chosen for reconstructing ODF from QBI reconstruction, two of which correspond to single population cases (ROI_1 and ROI_2), with the third located exactly inside the crossing of fibres (ROI_3; figure 8).

Figure 9 displays three-dimensional renderings of the min–max normalized ODF superimposed on the T2-weighted image. ODF plots corresponding to single-fibre population cases display one single lobe, while ODF plots corresponding to the crossing display two main orientations along the *x*- and *y*-axes. Detected orientations seem to be consistent with the underlying fibre directions (figures 10 and 11), even if imaging conditions (phantom design and gradient coil capacity) do not allow better SNR. In comparison, the diffusion tensor model provides the main eigenvectors, which are coherent with the fibre structure inside single population regions, but the model completely fails to describe regions containing fibre crossings (figure 7*d*).

(**b**) ***Deviation angle measurements***

In order to evaluate the deviation of main orientations of the ODF from the *a priori* orientations of rayon

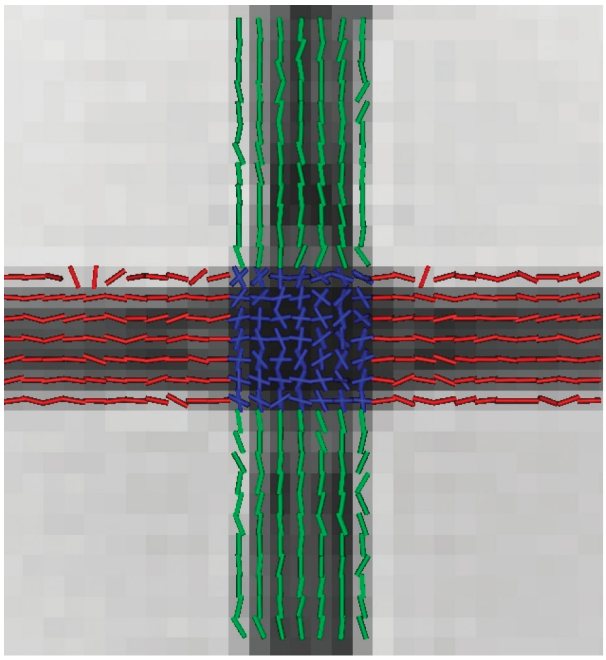

Figure 11. Main orientations of ODF calculated from QBI model. Red is used for representing orientations of ROI_1, green for orientations of ROI_2 and blue for orientations of ROI_3. Vectors for ROI_1 and ROI_2 are aligned with the *x*- and *y*-axis, respectively. ODF belonging to the fibre-crossing area present two main lobes, leading to both different orientations of the diffusion process that are globally consistent with the orientations of rayon fibres. This result must be compared with the eigenvector map of tensor model depicted in figure 7.

Table 1. Quadratic average deviation angle between the primary orientation of the ODF and the *x*- or *y*-laboratory axis in regions containing one single-fibre population (ROI_1 and ROI_2), or between the primary and second orientations of the ODF and both *x*- and *y*-axes in regions containing fibre crossing (ROI_3).
(*q*-Ball deviation angles can be compared with results obtained with diffusion tensor model.)

ROI, *a priori* orientation(s)	*q*-ball deviation angle (deg)	DTI deviation angle (deg)
ROI_1: $\boldsymbol{u}_x$	19.1	10.3
ROI_2: $\boldsymbol{u}_y$	15.5	10.0
ROI_3: ($\boldsymbol{u}_x$, $\boldsymbol{u}_y$)	29.8	53.4

fibres, we defined three regions of interest, two regions inside *x*- and *y*-bundles, and a third located inside the crossing area (figure 10). The deviation angles (table 1) for each of the three regions were evaluated as $\alpha_1 = 19.1°$ for the bundle oriented along the *x*-axis (ROI_1), $\alpha_2 = 15.5°$ for the bundle oriented along the *y*-axis (ROI_2) and $\alpha_3 = 29.8°$ for fibre crossing (ROI_3).

The same measurements were taken using the tensor model yielding the following results: the deviation angles for each of the three regions were evaluated to $\alpha_1 = 10.3°$ for the bundle oriented along the *x*-axis (ROI_1), $\alpha_2 = 10.0°$ for the bundle oriented along the *y*-axis (ROI_2) and $\alpha_3 = 53.4°$ for fibre crossing (ROI_3).

In the case of single population regions of interest, DTI seems to give better resolution than QBI. This is not surprising since the DTI model is reconstructed from a robust fit involving the only six coefficients of the tensor matrix, while QBI reconstruction is analytically model free, and, consequently, more sensitive to the presence of noise. We must keep in mind that imaging of diffusion phantoms is always more difficult than *in vivo* brain imaging, so the difference should be less striking with *in vivo* experiments. However, fibre-crossing locations clearly highlight the net contribution of QBI in comparison with DTI for describing multi-modal configurations in the case of *ex vivo* experiments (figures 7*d* and 11). However, the reliability of QBI *in vivo* has yet to be proved.

4. DISCUSSION

This study aimed to demonstrate the capability of QBI to describe the structural anisotropy of tissue more effectively than conventional DTI, by providing an accurate ODF, even in the context of clinical scanner use where imaging conditions are much less advantageous than for high gradient strength, short field of view MR systems, as used by Lin *et al.* (2003). Consequently, although it is not possible to reach orientation accuracy down to the degree order, QBI is sufficiently precise to allow studies of tissue orientation such as white matter fibre tracking or cytoarchitectony studies.

This accuracy relies primarily on scanner performance, phantom design and the QBI method.

The hardware limitations of the gradient coil in terms of maximum strength and slew-rate leads to an echo time not smaller than half of the T2 relaxation time, which directly decreases the SNR by a factor of two.

Phantom design also plays an important role in the SNR decrease. First, rayon fibres are permeable, but they do not have a tubular structure, such as myelinated axons. Therefore, the diffusion is largely restricted to the external cavity made up of the space between filaments. Consequently, the spin density of a voxel is drastically reduced compared with that of tubular structure, and the observed anisotropy remains low (fractional anisotropy was evaluated to 0.2 on FA map; figure 7*b*) because fibres were manually tightened. This manual operation does not allow for controlling of the average distance between fibres. Therefore, the average free random walk $\sigma = \sqrt{2D\tau} = 9.12\ \mu m$ may be too short compared with measuring a stronger anisotropy. The only possible action for improving this random walk observation is to increase the diffusion time τ. However, after several experiments, this potential solution was discarded because it also required increasing the echo time, resulting in a significant decline in SNR. Nevertheless, we were able to consistentently measure the anisotropy of the fibre-crossing structure on the diffusion phantom (figures 9–11). Such results confirm the efficiency of the QBI method for characterizing the structural orientation of tissue. Furthermore, it should be noted that white matter tissue is more suitable than textile fibres for diffusion imaging. This means that the quadratic angular error is probably much better than the 30° we reached with the diffusion phantom.

The QBI method itself affects the theoretical angular accuracy of the ODF. First, the number of diffusion

gradient orientations used during the acquisition influences *q*-ball reconstruction. The post-processing reconstruction relies on the integration of the MR signal around the equators of discrete orientations $\boldsymbol{u}$ of the ODF. Because it is unlikely that gradient orientations fall exactly on the different equators, an interpolation step of the MR signal is required to smooth the input data. This processing is also necessary for removing noise in the ODF. Unfortunately, however, this processing may mean that some structural information is lost. A low structural anisotropy can lead to variation of the signal comparable to hardware noise. In the phantom experiment, 200 non-collinear gradient orientations were selected. These form a uniform orientation set with 10.09° angular resolution between neighbours when symmetric orientations are taken into account. The number of equator sampling points was arbitrarily set to 100 and the ODF was evaluated at 1000 uniformly distributed points over a sphere, leading to a 6.45° angular resolution. The equator points' interpolation was performed using a Gaussian kernel regression with standard deviation equal to twice the angle between acquisition points (i.e. 20.18°). Prior to normalization, diffusion ODFs went through a last Gaussian smoothing step for removing remaining noise on unimodal ODFs. The width of the kernel was set to 20°, which corresponds approximately to three times the angular resolution of the ODF sampling scheme. Tuch (2004) demonstrated with simulations that the choice for this kernel width can be accurately determined for removing only sharp peaks without smoothing or merging true diffusion lobes.

The limitation of angular accuracy of ODF modes can also be explained by the approximation of the radial projection that is replaced by an integration over a cylindrical domain, introducing information about displacement probabilities not measured exactly along the concerned modes. In the phantom experiment, the diameter of the cylinder was evaluated as 10.7 μm (see §2). This radial spatial resolution results from a compromise between SNR and angular resolution. Since bundles are crossing at 90°, a poor radial spatial resolution does not significantly influence the position of main lobes of the ODF. In the future, it would be interesting to study the effects of this radial projection approximation more precisely.

In conclusion, the average angular resolution estimated between 15 and 30° according to the number of peaks to be detected seems to be reasonable compared with scanner performances, diffusion phantom realism and model assumptions. Further work has to be carried out for improving the quality of diffusion phantom.

Several other high angular resolution diffusion models are worth being tested, such as DSI (Tuch 2002), spherical deconvolution model (Tournier *et al.* 2004), maximum entropy solutions or persistent angular structure model (Alexander & Jansons 2002, Jansons & Alexander 2003) and the CHARMED model (Assaf *et al.* 2004). All algorithms have their own advantages and drawbacks, but QBI does not make any analytical assumption about the underlying structure. This is a significant advantage compared with other methods that depend on analytical expressions that often need strong structural assumptions in order to provide good convergence of reconstruction algorithms. However, as in other models, the QBI model is only able to describe some configurations of heterogeneous orientation structure. QBI can efficiently deduce fibre crossing when it corresponds to both bundles of almost equivalent size, but it fails, for instance, to depict fan configurations where fibres are splitting or merging, because anisotropy falls below the level of noise and angular resolution is not sufficient for describing the distribution of orientation peaks. In conclusion, it is important to point out that rayon phantom provides an excellent model to study fibre fanning or bending configurations.

The authors would like to thank Dr Paola Scifo for her helpful advice on fibre choice, and Dr Jean-Michel Hermel for providing microscopic acquisitions of rayon fibres.

REFERENCES

Alexander, D. C. & Jansons, K. M. 2002 *Spin echo attenuation to diffusion density: a general inversion for measurements on a sphere. ISMRM Workshop on Diffusion MRI, Saint-Malo,* pp. 206–209

Assaf, Y. & Cohen, Y. 1999 Structural information in neuronal tissue as revealed by q-space diffusion NMR spectroscopy of metabolites in bovine optic nerve. *NMR Biomed.* **12**, 35–44.

Assaf, Y., Freidlin, R. Z., Rohde, G. K. & Basser, P. J. 2004 New modeling and experimental framework to characterize hindered and restricted water diffusion in brain white matter. *Magn. Reson. Med.* **52**, 965–978.

Basser, P. J. 1995 Inferring microstructural features and the physiological state of tissues from diffusion-weighted images. *NMR Biomed.* **8**, 333–344.

Basser, P. 1998 Fiber-tractography via diffusion tensor MRI (DT-MRI). In *Proceedings of the Sixth ISMRM Conference, Sydney*, 2 p. 1226

Basser, P. J. 2002 Relationships between diffusion tensor and q-space MRI. *Magn. Reson. Med.* **47**, 392–397.

Basser, P. J. & Pierpaoli, C. 1996 Microstructural and physiological features of tissues elucidated by quantitative-diffusion-tensor MRI. *J. Magn. Reson. Ser. B* **111**, 209–219.

Basser, P. J., Mattiello, J. & LeBihan, D. 1994 MR diffusion tensor spectroscopy and imaging. *Biophys. J.* **66**, 259–267.

Behrens, T. E. *et al.* 2003 Non-invasive mapping connections between human thalamus and cortex using diffusion imaging. *Nature Neurosci.* **6**, 243–249.

Callaghan, P. T. 1988 NMR microscopy of dynamic displacements: *k*-space and *q*-space imaging. *J. Phys. E: Sci. Instrum.* **21**, 820–822.

Callaghan, P. T. 1991 *Principles of nuclear magnetic resonance microscopy.* Oxford: Oxford University Press.

Cointepas, Y., Poupon, C., Maroy, R., Rivière, D., LeBihan, D. & Mangin, J. F. 2003 A freely available Anatomist/-BrainVISA package for analysis of diffusion MR data. Proceedings of the Ninth HBM Scientific Meeting, New-York. *NeuroImage* **19**((Suppl. 2), 810 http://brainvisainfo/

Conturo, T. E., Lori, N. F., Cull, T. S., *et al.* 1999 Tracking neuronal fiber pathways in the living human brain. *Proc. Natl Acad. Sci. USA* **96**, 10 422–10 427.

FiberSource, http://www.fibersource.com/f-tutor/rayon.htm

Gory, D. G. & Garroway, A. N. 1990 Measurement of translational displacement probabilities by NMR: an indicator of compartmentation. *Magn. Reson. Med.* **14**, 435–444.

Grannel, P. K. & Mansfield, P. 1975 Microscopy in vivo by nuclear magnetic resonance. *Phys. Med. Biol.* **20**, 477–482.

Inglis, B. A., Bossart, E. L., Buckley, D. L., Wirth, E. D. & Mareci, T. H. 2001 Visualization of neural tissue water compartments using biexponential diffusion tensor MRI. *Magn. Reson. Med.* **45**, 580–587.

Jansons, K. M. & Alexander, D. C. 2003 Persistent angular structure: new insights from diffusion magnetic resonance imaging data. *Inverse Probl.* **19**, 1031–1046.

Jones, D. K., Horsfield, M. A. & Simmons, A. 1999 Optimal strategies for measuring diffusion in anisotropic systems by magnetic resonance imaging. *Magn. Reson. Med.* **42**, 515–525.

Jones, D. K., Simmons, A., Williams, S. C. & Horsfield, M. A. 2000 Non-invasive assessment of axonal fiber connectivity in the human brain via diffusion tensor MRI. *Magn. Reson. Med.* **42**, 37–41.

LeBihan, D. 1991 Molecular diffusion nuclear magnetic resonance imaging. *Magn. Reson. Q.* **7**, 1–30.

LeBihan, D. & Basser, P. J. 1995 Molecular diffusion and nuclear magnetic resonance. In *Diffusion and perfusion magnetic resonance imaging: applications to functional MRI* (ed. D. LeBihan), pp. 5–17. New York: Raven Press.

LeBihan, D., Breton, E. & Lallemand, D. 1986 MR imaging of intravoxel incoherent motions: application to diffusion and perfusion in neurologic disorders. *Radiology* **161**, 401–407.

Lin, C. P., Wedeen, V. J., Chen, J. H., Yao, C. & Tseng, W. Y. I. 2003 Validation of diffusion spectrum magnetic resonance imaging with manganese-enhanced rat optic tracts and ex vivo phantoms. *NeuroImage* **19**, 482–495.

Mansfield, P. & Grannel, P. K. 1973 NMR diffraction in solids. *J. Phys. C* **6**, L422–L426.

Mitra, P. P. & Halperin, B. I. 1995 Effects of finite gradient-pulse widths in pulsed-field gradient diffusion measurements. *J. Magn. Reson. A* **113**, 94–101.

Mori, S., Kaufman, W. E., Pearlson, G. D., *et al*. 2000 In vivo visualization of human neural pathways by magnetic resonance imaging. *Ann. Neurol.* **47**, 412–414.

Moseley, M. E., Cohen, Y. & Mintorovitch, J. 1990 Early detection of regional cerebral ischemic injury in cats: evaluation of diffusion and T2-weighted MRI and spectroscopy. *Mag. Reson. Med.* **14**, 330–346.

Niendorf, T., Dijkhinzen, R. M., Norris, D. G., Looheren Campagne, M. & Nicolay, K. 1996 Biexponential diffusion attenuation in various states of brain tissue: implications for diffusion-weighted imaging. *Magn. Reson. Med.* **36**, 847–857.

Pajevic, S. & Pierpaoli, C. 1999 Color schemes to represent the orientation of anisotropic tissues from diffusion tensor data: application to white matter fiber tract mapping in the human brain. *Magn. Reson. Med.* **42**, 526–540.

Parker, G. J. & Alexander, D. C. 2003 Probabilistic Monte Carlo based mapping of cerebral connections utilising whole-brain crossing fiber information. *Inf. Process. Med. Imaging* **18**, 684–695.

Parker, G. J. M. & Alexander, D. C. 2005 Probabilistic anatomical connectivity derived from the microscopic persistent angular structure of cerebral tissue. *Phil. Trans. R. Soc. B* **360**, 893–902. (doi:10.1098/rstb.2005.1639.)

Pfeuffer, J., Flogel, U., Dreher, W. & Leibfritz, D. 1998 Restricted diffusion and exchange of intracellular water: theoretical modelling and diffusion time dependence of H NMR measurements on perfused glial cells. *NMR Biomed.* **11**, 19–31.

Pierpaoli, C. & Basser, P. J. 1996 Toward a quantitative assessment of diffusion anisotropy. *Magn. Reson. Med.* **36**, 893–906.

Poupon, C., Mangin, J.-F., Frouin, V., Regis, J., Poupon, F., Pachot-Clouard, M., LeBihan, D. & Bloch, I. 1998 Regularization of MR diffusion tensor maps for tracking brain white matter bundles. In *Proceedings of the First MICCAI Conference, Cambridge*, pp. 489–498. New York: Springer.

Poupon, C., Mangin, J.-F., Frouin, V., Regis, J., LeBihan, D. & Bloch, I. 2000 Toward inference of human brain connectivity. *NeuroImage* **12**, 184–195.

Stejskal, E. O. 1965 Use of spin echoes in a pulsed magnetic field gradient to study restricted diffusion and flow. *J. Chem. Phys.* **43**, 3597–3603.

Stejskal, E. O. & Tanner, J. E. 1965 Spin diffusion measurements: spin echoes in the presence of a time-dependent field gradient. *J. Chem. Phys.* **42**, 288–292.

Tanner, J. E. & Stejskal, E. O. 1968 Restricted self-diffusion of protons in colloidal systems by the pulsed-gradient, spin echo method. *J. Chem. Phys.* **49**, 1768–1777.

Tournier, J. D., Calamante, F., Gadian, D. G. & Connelly, A. 2004 Direct estimation of the fiber orientation density function from diffusion-weighted MRI data using spherical deconvolution. *NeuroImage* **23**, 1176–1185.

Tuch, D. S. 2002 Diffusion MRI of complex tissue structure. PhD thesis, Harvard-MIT.

Tuch, D. S. 2004 Q-ball imaging. *Magn. Reson. Med.* **52**, 1358–1372.

Tuch, D. S., Reese, T. G., Wiegell, M. R., Makris, N., Belliveau, J. W. & Wedden, V. J. 1998 High angular resolution diffusion imaging reveals intravoxel white matter fiber heterogeneity. *Magn. Reson. Med.* **48**, 577–582.

Wiegell, M. R., Tuch, D. S., Larsson, H. B. W. & Wedeen, J. 2003 Automatic segmentation of thalamic nuclei from diffusion tensor magnetic resonance imaging. *NeuroImage* **19**, 391–401.